AIAA JOURNAL
Vol. 48, No. 11, November 2010

Large Eddy Simulation and Experimental Study of a Controlled Coaxial Liquid-Air Jet

Nicolas Guézennec* and Thierry Poinsot†
Institut de Mécanique des Fluides de Toulouse, 31400 Toulouse, France

DOI: 10.2514/1.J050416

This paper describes the numerical and experimental study of the control of the trajectory and spreading of an air-assisted water spray. The configuration is a coaxial set up where the liquid injected by the central tube is atomized by a surrounding high-speed annular air flow. This spray is actuated in its outlet plane using additional air jets to modify either its trajectory or its spreading angle (by adding swirl). Large eddy simulation is used jointly with experimental measurements (hot-wire anemometry for the air flow without spray and phase Doppler anemometry for the spray cases) to analyze the flow with and without control. Results show that 1) large eddy simulation of two-phase flows using a Lagrangian solver is a precise method to predict such flows, and 2) the spray jet can be effectively modified using simple actuators, suggesting that the same devices applied to fuel sprays in combustion chambers, would be an effective active control actuator. Large eddy simulation results also reveal the complex flow patterns and effects on droplet distribution induced by the actuators and appear as an excellent tool to complement and understand experimental data.

I. Introduction

THE present work focuses on two issues which are important for liquid-fuel combustion chambers and more generally for two-phase flows systems:

1) Active control of combustion [1,2] continues to be studied to suppress combustion instabilities, optimize combustion efficiency or minimize pollutant emissions. The list of actuators which can be imagined for combustors has no limit [3–9] and the introduction of electronics in the regulation of combustors allows to design 'smart' combustors which can be operated with a variety of active control systems. In liquid-fueled combustors, actuating the fuel spray entering the chamber is a logical approach in most cases because it requires a limited energy and has a potentially strong effect on the flow since it changes the local mixing and combustion intensity. Understanding how active control devices modify the spray and the combustor flow is often a difficult task and simulations of controlled combustors are very rare.

2) Independent of the combustor control systems, being able to predict its performances using simulations is an obvious target for many computational fluid dynamics (CFD) teams. In the recent years, large eddy simulation (LES) have demonstrated their power to predict complex reacting gaseous flows even in realistic geometries [10–13]. The application of these methods to two-phase flames is much more difficult [14–16]. Simply being able to predict the performances of uncontrolled combustors is a daunting task for most LES practioneers so that using LES to predict the performances of active control devices applicable to liquid-fueled combustors is a virtually untouched topic.

The objective of the present work is to explore these two issues by studying active control of sprays on a simple experiment, representative of fuel sprays formed in combustion chambers. We will test whether LES of the actuated spray, using a Lagrangian formulation, can be used to predict the performances of two actuators: the first one (Dev) is used to modify the trajectory of the spray while the second one (Sw) introduces swirl into the spray to modify its spreading rate and mixing with the surrounding air. In both cases, the actuators are small rectangular jets added in the outlet plane of the spray generator. The baseline uncontrolled spray is created in a coaxial set up where a liquid column issued from the central tube is assisted by a high-speed annular air flow. The air feeding the coaxial atomizing stream and the control rectangular jets is the same. Although this configuration is simpler than injectors found for example in gas turbine combustors (which use multiple air passages and complex liquid injectors), it is an excellent research tool to initiate such studies. It is also close to spray systems used to atomize liquid fuels in certain industrial combustors like glass-melting, aluminum-melting or steel-reheat furnaces.

Active control is often viewed as an exercise where the energy of the actuator must be kept to a minimum and the flow rate used in the actuators must remain small. Here, the context is different: in most combustion chambers, the problem is not to spend energy to introduce additional air for control but more to split the available air differently. We will consider that the total flow rate of air available to produce the spray is constant and can be split in two parts: the main atomizing air used in the uncontrolled configuration and the control air feeding the actuation jets. The sum of these two flow rates is imposed but the distribution is free so that large amounts of air can be diverted from the main stream to the actuation air: typically, up to 40% of the total air flow rate will be allowed to flow through the actuation jets in this study. Even though these values exceed these commonly found for external aerodynamics where control must be obtained with low forcing levels, they can be obtained easily in combustion chambers where the total air flow rate can be distributed arbitrarily. Many results presented in the present paper show actuation effects which are very strong: the first-order reason for this is not the introduction of smarter actuators but the fact that more energy was used for these actuators.

Section II describes the experimental setup and the actuators geometry. Experimental methods (hot-wire anemometry and phase Doppler anemometry (PDA) are described and the LES solver is briefly presented before focusing on the method used to introduce the liquid particles in the LES. Section III describes the results of the LES with and without control in the absence of spray while Sec. IV presents the results obtained with spray.

II. Simulation and Experimental Approach

A. Flow Configuration

The injector geometry is presented on Fig. 1a. Water is injected in the inner pipe. Air is injected between the two nozzles to atomize the liquid flow. The first configuration without any actuation system (Coax) is used as the reference case.

Received 4 January 2010; revision received 26 May 2010; accepted for publication 11 June 2010.

*INP de Toulouse.
†Research Director, INP de Toulouse and CNRS. Associate Fellow AIAA.

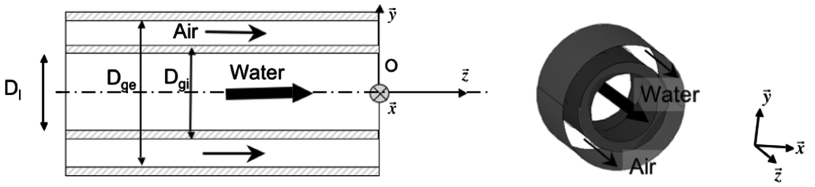

a) Coaxial injector (Coax): geometrical dimensions and 3D visualisation

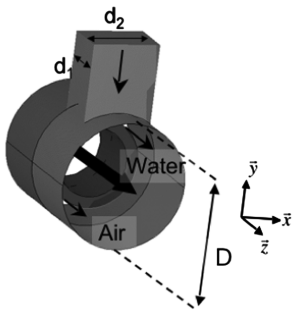

b) 3D visualisation of the injector with the vectoring control system (Dev)

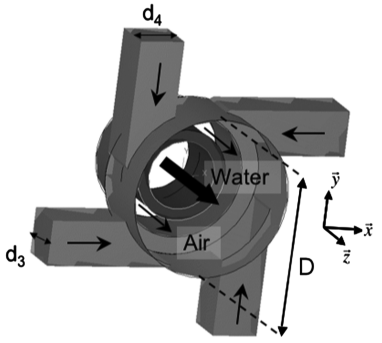

c) 3D visualisation of the injector with the swirl control system (SW)

Fig. 1 Schematic of the flow configurations.

The actuators are rectangular air jets disposed around the injector exit (Figs. 1b and 1c). Two configurations are explored (Table 1): the first one (Dev) uses a unique radial actuator which vectors the main flow (Fig. 1b). The second configuration (Sw) is composed of four tangential jets to add swirl to the flow (Fig. 1c).

The liquid and atomization flow rates are constant. The liquid Reynolds number Re_l is 3000 and the flow is laminar (Farago and Chigier [17]). The gas Reynolds number Re_g is 30,000 and corresponds to a bulk velocity $U_{g\text{inj}}$ of 166 m/s for the uncontrolled case (Coax). For configurations with control, the total mass flow rate is separated between the injector flow rate $\dot{m}_{\text{inj}}$ and the actuators $\dot{m}_{\text{ac}}$:

$$\dot{m}_g = \dot{m}_{\text{inj}} + \dot{m}_{\text{ac}} \tag{1}$$

The control intensity is characterized by the parameter R_{ac}:

$$R_{\text{ac}} = \dot{m}_{\text{ac}}/\dot{m}_g \tag{2}$$

R_{ac} is, respectively, set equal to 0.2 and 0.4 for the configurations (Dev) and (Sw), corresponding to bulk velocities $U_{g\text{ac}}$ in the actuators of 66 m/s and 35 m/s, respectively. They are kept constant throughout this paper. Table 2 summarizes all characteristic dimensions and flow parameters.

B. Experimental Techniques

The first test facility was dedicated to gas velocity measurements with hot-wire anemometry without spray. The second facility was used to perform phase Doppler anemometry (PDA) measurements on the spray and provide droplet size and velocity distributions.

The instantaneous velocity measured by the hot-wire probe is noted u_{hw}. It is the sum of the three velocity components following the Jorgensen's equation [18]:

$$u_{\text{hw}}^2 = u_z^2 + k^2 u_y^2 + h^2 u_x^2 \tag{3}$$

with $k = 1.05$ and $h = 0.2$. In the reference case of the coaxial jet (Coax) u_y and u_x are small compared with u_z in most parts of the flow, so that the hot-wire response nearly corresponds to the norm of the axial velocity u_z. For the configurations (Dev) and (Sw), however, the actuators induce non negligible transverse velocity components and the hot-wire velocity u_{hw} is not equal to the axial velocity u_z.

For PDA, at each measurement point, the instantaneous axial velocity u_{zp} and the diameter d_p are recorded for 50000 droplets.

Table 1 List of cases

Name	Setup	Objective
(Coax)	No actuator	Reference case
(Dev)	One impacting jet	Vectored jet : change trajectory
(Sw)	Four tangential jets	Swirled flow : increase mixing

C. Numerical Setup

1. Gaseous Phase

All simulations are fully three-dimensional compressible LES performed with an explicit LES solver [19,20] using a second-order finite volume Lax–Wendroff scheme. The solver uses the classical Smagorinsky approach [21] to model the subgrid stress tensor and the NSCBC method [22] for boundary conditions. To compare simulations with hot-wire measurements, a numerical value of u_{hw} is computed from the LES resolved field using Eq. (3). Subgrid scale velocity fluctuations are neglected when computing the rms value of the LES velocity u_{hw}.

2. Dispersed Phase: Euler–Lagrange Approach

The dispersed phase is solved in the LES using a Lagrangian approach where droplets are assumed to be rigid spheres with diameter comparable or smaller than the Kolmogorov length scale. Typically, 1.5 million droplets were tracked simultaneously in the LES. Because the liquid density is much larger than the fluid density ($\rho_p/\rho_g \gg 1$), the forces acting on particles reduce to drag and

Table 2 Characteristic dimensions and flow parameters

	(Coax)	(Dev)		(Sw)	
D_l, mm		3			
D_{gi}, mm		4			
D_{ge}, mm		5.5			
$\dot{m}_l$, g/s		6.8			
U_l, m/s		0.962			
$\dot{m}_g$, g/s		2.14			
Actuators	0	1		4	
Dimensions, mm	——	d_1	d_2	d_3	d_4
	-	2	3	2	2
D, mm	5.5	5.5		7	
R_{ac}	0	0.2		0.4	
$U_{g\text{inj}}$, m/s	166	130		100	
$U_{g\text{ac}}$, m/s	0	66		35	

gravity [23,24]. Collisions and secondary atomization are neglected: neglecting collisions is justified in the largest part of the domain but not near the injector, where the volume mass fraction can reach 0.2. However, considering the limited level of accuracy in this region and the high cost of collision treatments in Lagrangian methods [25–28], this mechanism was simply neglected. Regarding secondary atomization, droplet Weber numbers will be evaluated a posteriori using LES data and shown to be small enough to avoid atomization in most of the domain (Sec. IV.A). In Lagrangian simulations, the influence of particles on the gas-phase momentum and energy equations is taken into account by using the point-force approximation in the general framework of the particle-in-cell method (PIC) [29–33], with standard single-phase subgrid turbulence modeling approaches.

Under these assumptions, the particle equations of motion are written for a single particle as:

$$\frac{\mathrm{d}x_{p,i}}{\mathrm{d}t} = u_{p,i} \tag{4}$$

$$\frac{\mathrm{d}u_{p,i}}{\mathrm{d}t} = -\frac{3}{4}\frac{\rho_g}{\rho_p}\frac{C_D}{d_p}|\mathbf{v}_r|v_{r,i} + g_i = -\frac{u_{p,i} - \tilde{u}_{g,i}}{\tau_p} + g_i \tag{5}$$

with g_i the gravity vector. The particle relaxation time τ_p is defined as the Stokes characteristic time:

$$\tau_p = \frac{4}{3}\frac{\rho_p}{\rho_g}\frac{d_p}{C_D|\mathbf{v}_r|} \tag{6}$$

The local drag coefficient C_D in Eq. (5) is expressed in terms of the particle Reynolds number Re_p following Schiller and Nauman [34]:

$$C_D = \frac{24}{Re_p}[1 + 0.15Re_p^{0.687}] \quad \text{for } Re_p = \frac{|\mathbf{v}_r|d_p}{\nu_g} \leq 800 \tag{7}$$

where d_p is the particle diameter and ν_g is the kinematic viscosity of the gas phase. The local instantaneous relative velocity between the particle and the surrounding fluid is $v_{r,i} = u_{p,i} - \tilde{u}_{g,i}$, where $\tilde{u}_{g,i}$ is the fluid velocity at the position of the particle assuming that the flow field is locally undisturbed by the presence of this particle [24,35]. The gas velocity at the droplet location is assumed to be equal to the interpolated filtered velocity at the position of the particle [36–38]. The effect of subgrid fluctuations is neglected.

3. *Meshes and Boundary Conditions*

LES simulations have been performed with and without spray for the three experimental configurations (Coax), (Dev) and (Sw) of Table 1. Experimental geometries have been slightly simplified but they all include the zone where actuators are mounted (cf. Figure 2). The reference point O is at the center of the injector exit (Fig. 1a). For the gaseous computations (without spray), the liquid pipe extremity is replaced by a wall while it corresponds to the plane of liquid injection for spray computation (cf. Figure 3). For the configuration (Coax) the injector duct length is 6 mm (Fig. 2a). For the configurations (Dev) and (Sw) the injector and actuators pipes are shortened to 3 mm (Figs. 2b and 2c). For all configurations, the rest of the computational domain is a cylinder with a radius $R_{\mathrm{box}} = 0.1$ m and a length $L_{\mathrm{box}} = 0.2$ m. Geometries are meshed using unstructured tetrahedra. The refinement is maximal in the injector and the actuators with a minimal cell volume around 10^{-13} m^3 (Table 3). Such fine meshes correspond to the limit of the point-source approximation used to track droplets: the maximum droplet size is of order of 100 μm where the smallest mesh size is 200 μm. Obviously, Lagrangian simulations are reaching a limit here: present meshes allow to decrease the mesh size to values which are of the order of the droplet size. This means that the point-source approximation may be invalid in the most refined parts of the grid. This question was beyond the scope of the present work.

Synthetic turbulence is imposed at the inlet of the injector and the actuators (Sec. I and 1_{ac}). The mean axial velocity profile is built following the classical 1/7 power law. An isotropic turbulent perturbation is constructed using a random flow generation algorithm [39,40] and added to the incoming mean flow. The turbulent intensity is 10% and the integral length scale equal to 0.4 mm. To inject turbulence without generating noise at the inlet or creating reflections of acoustic waves, the nonreflecting boundary condition developed

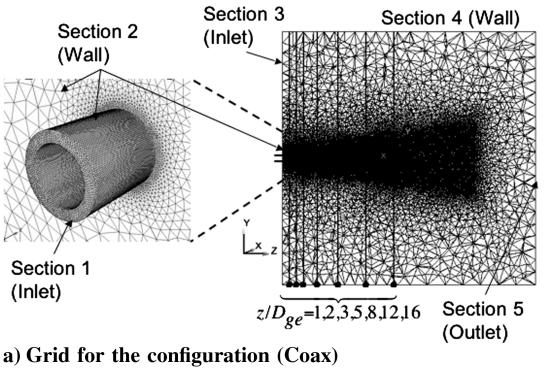

a) Grid for the configuration (Coax)

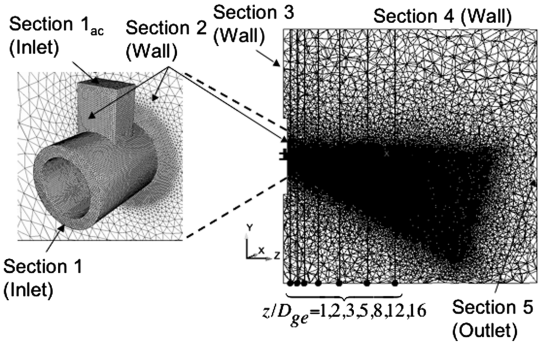

b) Grid for the configuration (Dev)

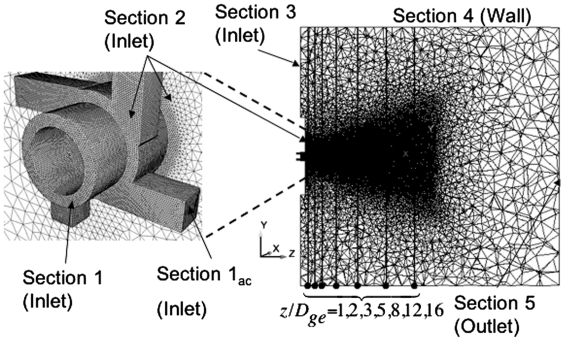

c) Grid for the configuration (Sw)

Fig. 2 Grids for the three configurations.

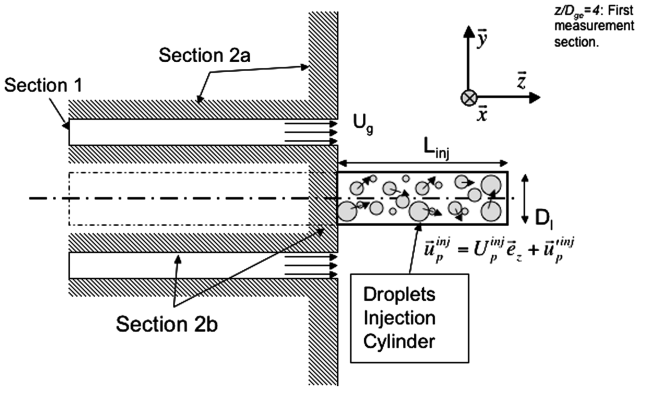

Fig. 3 Injection of droplets.

Table 3 Computational grid properties

	Coax	Dev	Sw
Cells	5019217	3661088	4961307
Nodes	86603	634877	861206
Minimal cell volume, m^3	1.1e-13	1.01e-13	9.1e-14
CPU time, h	20000	11000	20000
Processors	384	384	384

by Guézennec and Poinsot [41] for turbulence injection in compressible flows is used. A logarithmic law-of-the-wall is imposed on the walls of the injector and of the actuators (Sec. II).

A very slow laminar coaxial flow (0.1 m/s) is imposed on the inlet of the computation box (Sec. III) using a semireflecting characteristic boundary condition [22]. The lateral surface is an adiabatic slip-wall and the outlet is nearly nonreflecting at atmospheric pressure.

4. Methodology for Droplet Injection

Primary atomization can not be studied with the present method and the LES begins after this zone. Particles are injected within a cylinder at the exit of the liquid pipe (Fig. 3). The diameter of the injection cylinder is $D_{\text{inj}} = D_l$ and its length is $L_{\text{inj}} = 1.7D_l$ corresponding to the typical length of the liquid core for the superpulsating mode of a coaxial injector [42–44].

The distribution of droplet diameters can be fitted using a log-normal law based on two parameters: the injected mean and rms diameters D_{10}^{inj} and $D_{\text{RMS}}^{\text{inj}}$. A direct measurement of these two quantities in the injection plane with PDA is not possible since the spray is too dense in this zone. Therefore, these two parameters are estimated using the closest experimental data to the injector at $z/D_{ge} = 4$. They are obtained by averaging all droplets measured with the PDA at $z/D_{ge} = 4$. Figure 4 compares the injected log-normal distribution with the experimental pdf of all droplets measured at $z/D_{ge} = 4$ for (Coax). The agreement is good except around $d_p = 20$ μm where f_n is underestimated by the log-normal interpolation. For the three configurations, the coaxial atomizer generates a large range of droplet sizes. Therefore, the diameter distribution was split in four size classes: 1) $d_p < 20$ μm, 2) 20 $\mu\text{m} \le d_p < 50$ μm, 3) 50 $\mu\text{m} \le d_p < 100$ μm, and 4) 100 $\mu\text{m} \le d_p$. Dashed vertical lines on Fig. 4 indicate the separation between classes. For the biggest droplets in class 4, the LES was not long enough to provide perfectly converged data and no results will be presented for class 4) in the rest of the paper.

Table 4 gives the particle relaxation time τ_p depending on the particle diameter d_p. Assuming Stokes flow around particles, τ_p is given by

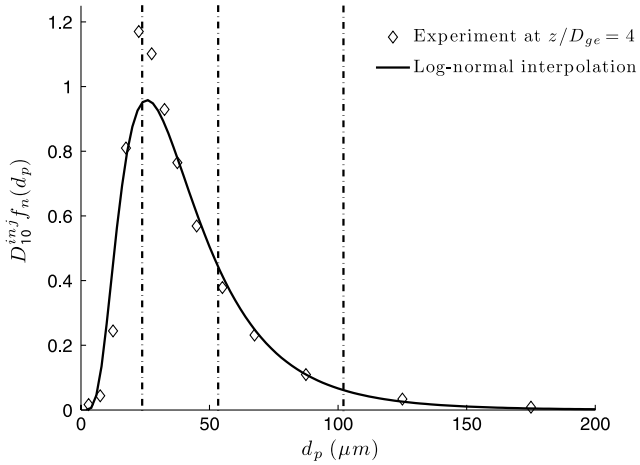

Fig. 4 Inflow conditions for the number distribution $f_n(d_p)$. Comparison between the experimental distribution at $z/D_{ge} = 4$ and the prescribed Log-normal interpolation for (Coax).

Table 4 Particle relaxation time and Stokes number depending on particle diameter in the injection zone ($z < L_{\text{inj}}$)

Size Class	1		2		3	
d_p, μm	10	20	35	50	75	100
τ_p, ms	0.3	1.3	3.9	7.9	17.8	31.7
St	2.9	11.5	35.1	71.7	161	287

Table 5 Injection of droplets

	Coax	Dev	Sw
D_{10}^{inj}, μm	43	50	50
$D_{\text{RMS}}^{\text{inj}}$, μm	33	40	48
D_{min}, μm		3	
D_{max}, μm		200	
W_p^{inj}, m/s		10	
$u_{p\,\text{max}}^{\prime\text{inj}}$, m/s		10	

$$\tau_p = \frac{\rho_p d_p^2}{18\mu_g} \tag{8}$$

where μ_g is the viscosity of air. The comparison of τ_p with a characteristic time scale of the fluid most energetic eddies τ_g yields the Stokes number St. For (Coax), the length of the most energetic eddies is estimated as a third of the injector diameter D_{ge}. In the injection plane, their velocity is estimated from the turbulence intensity, which is typically 10% of the bulk velocity $U_{g\text{inj}}$ close to the injector

$$\tau_g = \frac{D_{ge}/3}{0.1U_{g\text{inj}}} = 0.11 \text{ ms} \tag{9}$$

Table 4 shows that most droplets have a Stokes number greater than 1 and their trajectories are nearly independent from the gas flow in the injection zone.

The specification of the velocity field of the injected droplets is a difficult exercise. The velocity vector of each injected drop is

$$\mathbf{u}_p^{\text{inj}} = W_p^{\text{inj}}\mathbf{e}_z + \mathbf{u}_p^{\prime\text{inj}} \tag{10}$$

where W_p^{inj} is the mean injected velocity which is purely axial because of the large value of the gas velocity which constrains the liquid core. More sophisticated models would require to account for radial velocities but they were not included here [45]. Since the Stokes numbers of all droplets are large in the injection zone (Table 4), the fluctuations added on the droplet velocities are uncorrelated with the gas turbulent velocities fluctuations. Therefore, $\mathbf{u}_p^{\prime\text{inj}}$ can be expressed as a three-dimensional white noise with a maximal amplitude $u_{p\,\text{max}}^{\prime\text{inj}}$ for each cartesian direction. Table 5 presents the values of the parameters used to inject particles for each configuration. The values of W_p^{inj} and $u_{p\,\text{max}}^{\prime\text{inj}}$ were evaluated from the closest measurement points ($z/D_{ge} = 4$) and kept fixed for all LES.

III. Characterization of Control on the Air Flow

Before describing the effects of actuation on the liquid jet, it is useful to characterize the effects of control on the carrier phase (air) without spray. This is done in this section by using both simulation and experiments in the case where no liquid is injected.

A. Effects of Actuators on the Carrier Phase

Figures 5–7 present experimental and LES fields of the gas mean velocity U_{hw} and rms velocity $U_{\text{hw}}^{\text{RMS}}$ for the three configurations (Coax), (Dev) and (Sw). Without control, the jet contours are axisymmetric (Fig. 5), but the use of one impacting actuator for (Dev)

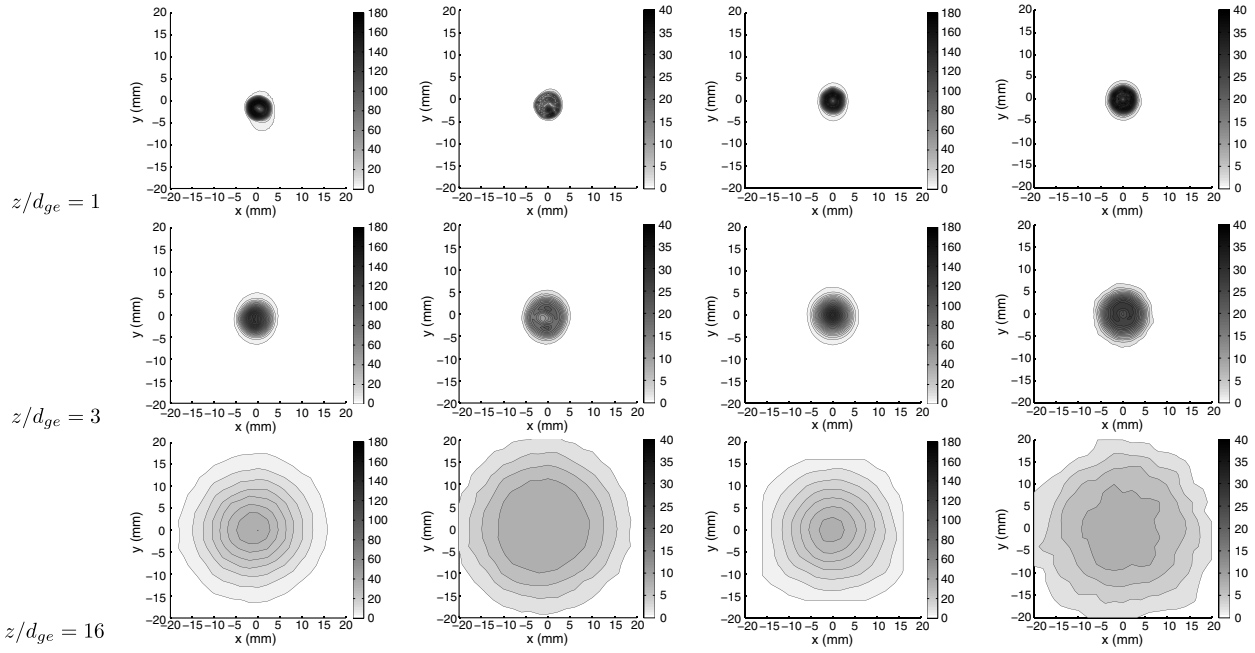

a) Experiment : U_{hw} **b) Experiment : U_{hw}^{RMS}** **c) LES : U_{hw}** **d) LES : U_{hw}^{RMS}**

Fig. 5 (Coax): Hot-wire mean and rms velocity fields. Comparison of Experiment and LES.

[Fig. 6] generates heart-shaped contours close to the injectors. The flow then evolves into an elliptic jet, significantly shifted from the initial jet axis. For the swirl configuration (Sw) [Fig. 7], even if actuators are placed symmetrically around the injector, they provide an helicoidal pattern to the jet. Experimental and numerical fields also reveal a rotating pattern around the axis of the jet suggesting a spiraling motion around **z**.

Line profiles at $x = 0$ are presented on Figs. 8–10. For each configuration, LES profiles are in good agreement with experimental data. Only a small overshoot of rms velocity is observed in the near field of the jet ($z/D_{ge} \leq 3$). These overshoots may be caused by the limited resolution of the mesh at the exit of the injector. The Smagorinsky subgrid model becomes ineffective to correctly predict the development of turbulent structures in this zone [46].

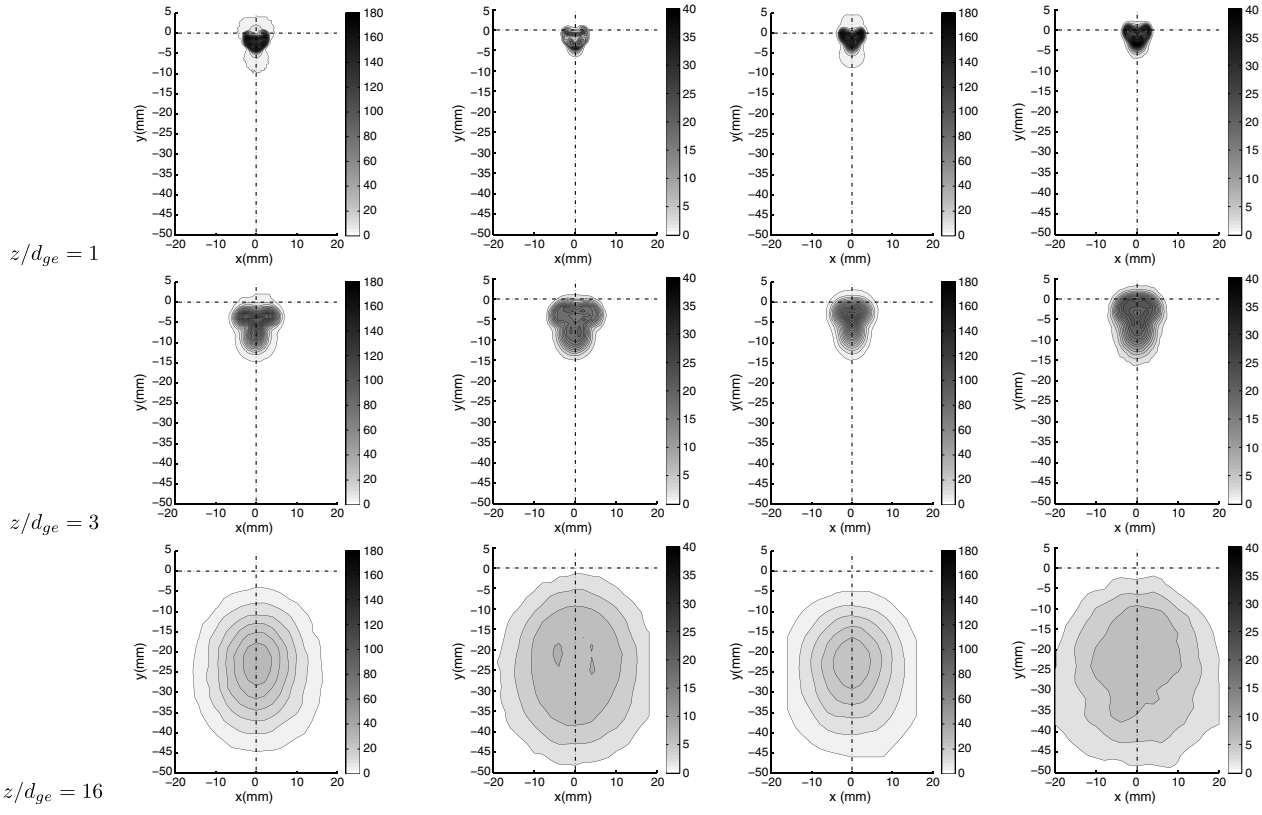

a) Experiment : U_{hw} **b) Experiment : U_{hw}^{RMS}** **c) LES : U_{hw}** **d) LES : U_{hw}^{RMS}**

Fig. 6 (Dev): Hot-wire mean and rms velocity fields. Comparison of Experiment and LES.

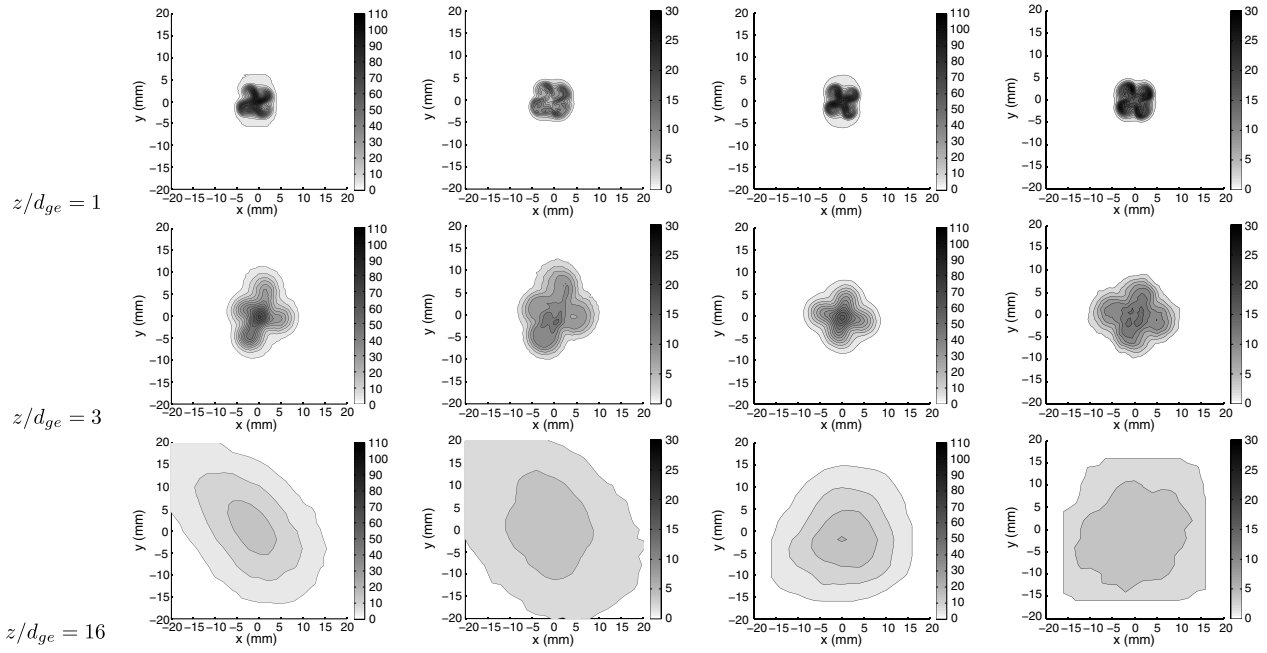

a) Experiment : U_{hw} **b) Experiment : U_{hw}^{RMS}** **c) LES : U_{hw}** **d) LES : U_{hw}^{RMS}**

Fig. 7 (Sw): Hot-wire mean and rms velocity fields at $z/D_{ge} = 1, 3, 16$. Comparison of experiment and LES.

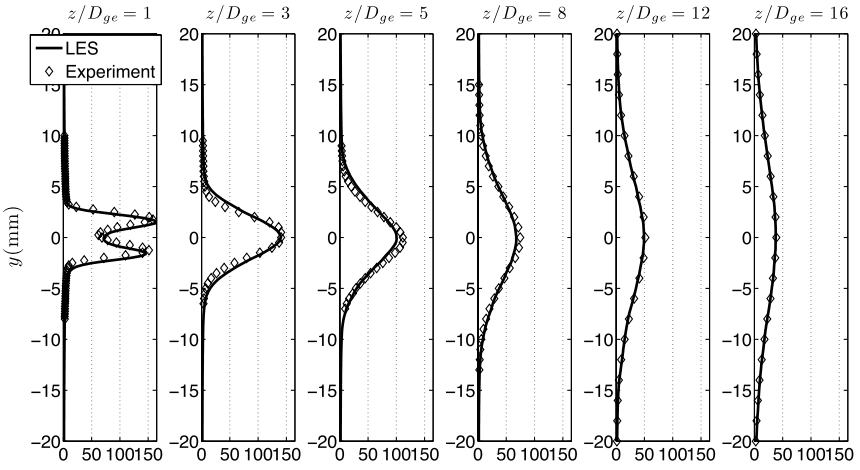

a) U_{hw}

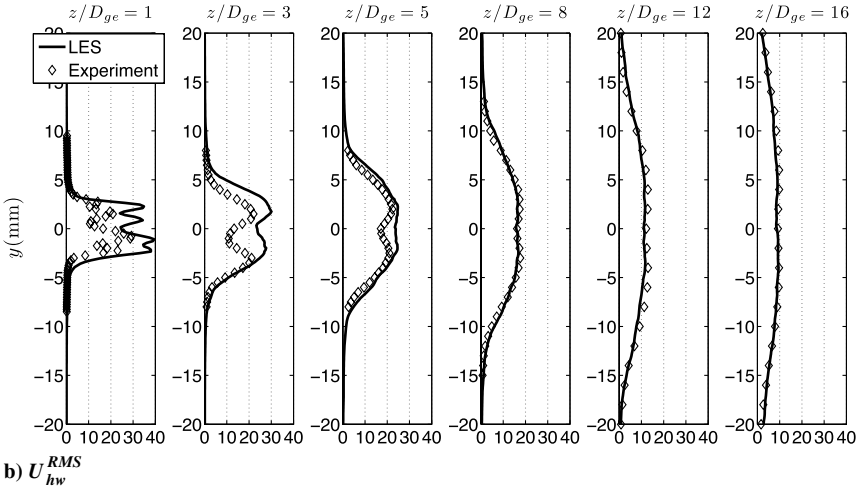

b) U_{hw}^{RMS}

Fig. 8 Profiles of mean velocity (top) and rms velocity (bottom) at $x = 0$ for (Coax). Comparison between LES and experiment.

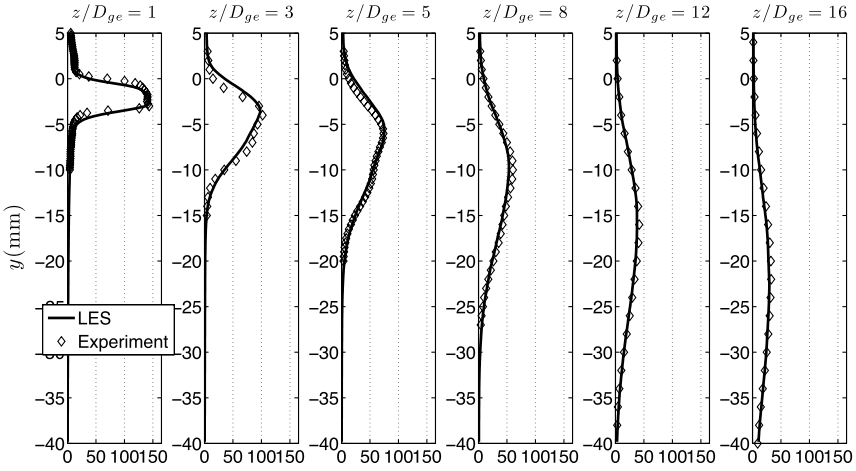

a) U_{hw}

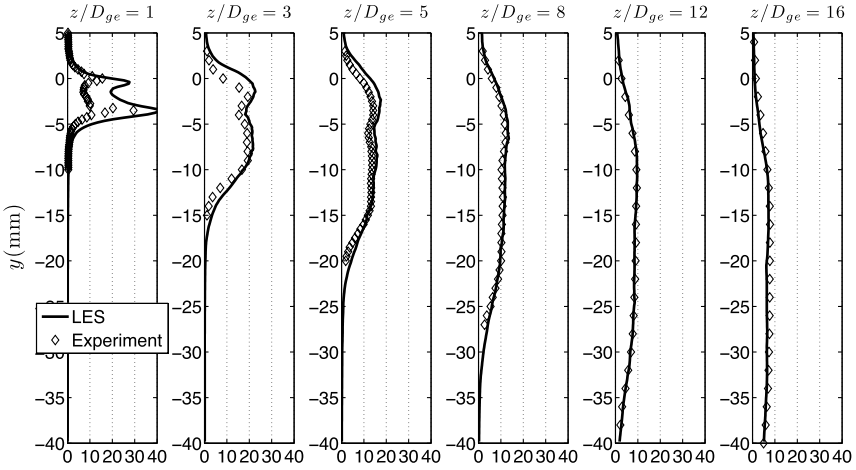

b) U_{hw}^{RMS}

Fig. 9 Profiles of mean velocity (top) and rms velocity (bottom) at $x = 0$ for (Dev). Comparison between LES and experiment.

For the configuration (Dev), the jet axis is can be identified from the position of the maximal mean velocity $y_{\max}$. This definition leads to a shift angle of the jet axis $\alpha_g^{\text{Dev}} = 15.1°$. Concerning (Sw), the jet expansion is estimated with the overexpansion ratio λ_g^{Sw} which compares the half width of the LES profiles of U_{hw} for (Coax) and (Sw)

$$\lambda_g^{\text{Sw}} = \frac{y_{0.5}^{\text{Sw}} - y_{0.5}^{\text{Coax}}}{y_{0.5}^{\text{Coax}}} \tag{11}$$

The expansion ratio λ_g^{Sw} is equal to 0.37 for $z/D_{ge} = 3$. However, this effect decreases further in the jet and for $z/D_{ge} = 12$, the half-widths of the jets for (Coax) and (Sw) are nearly equal. This phenomenon is due to the fact that for the control rate $R = 0.4$, swirl effects are still low.

B. Flow Structures Induced by Control

Figures 11–13 present the intensity and the vector field of U_{xy}: the LES mean velocity projected on the planes $z/D_{ge} = 0.75$ and $z/D_{ge} = 4$ respectively for (Coax), (Dev), and (SW2). For the configuration (Coax) (Fig. 11), U_{xy} essentially reveals a radial flow corresponding to the expanding jet. At $z/D_{ge} = 0.75$, the jet expansion is piloted by entrainment to the center of the jet, but at $z/D_{ge} = 4$, it is also due to entrainment from the center of the jet to its periphery. Actuators complicate the nature of entrainment in the jet: for (Dev) [Fig. 12], the impacting jet generates high **y** velocity levels around the jet center. This zone is surrounded by two counter-rotating vortices. For the swirled configuration (Sw) [Fig. 13], the actuators generate four corotating vortical structures. These vortices constitute the blades of the propeller shape observed on fields of Fig. 7. These four structures interact and generate a fifth central vortex which explains the spiraling motion of the jet around its axis **z**. An estimation from Fig. 13 gives a rotation angle equal to 63° between $z/D_{ge} = 0.75$ and $z/D_{ge} = 4$, which corresponds to an angular step of 3.5°/mm.

IV. Characterization of Control on the Spray

The effects of the actuators on the carrier phase have been described in the previous section. Tests are now repeated with liquid injection in the central duct of Fig. 1a.

A. Euler–Lagrange LES of the Controlled Spray

Figure 14 displays LES instantaneous snapshots in the planes $x = 0$ (left) and $z/D_{ge} = 16$ (right) for the uncontrolled case (Coax). Figure 14 shows the axial gas velocity contours and the corresponding snapshots for spray droplets. Each size class is represented with a different color: black for 1), gray for 2) and white for 3). As expected, without control, the droplets are dispersed by the coaxial air jet and the spray remains axisymmetric.

The LES was performed by assuming that secondary atomization was negligible. This assumption can now be checked from the LES data by computing the local Weber number We for the uncontrolled case and each size class:

$$We = \frac{\rho_g(\tilde{u}_z - W_p^i)^2 D_{10}^i}{\sigma} \tag{12}$$

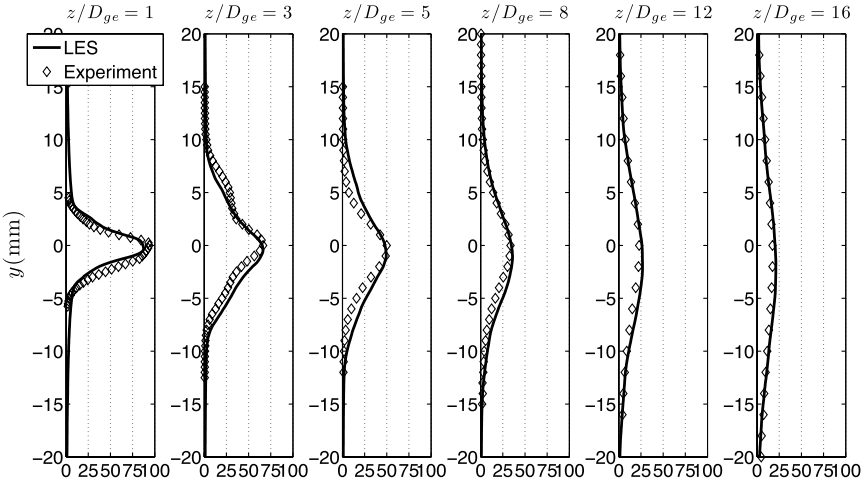

a) U_{hw}

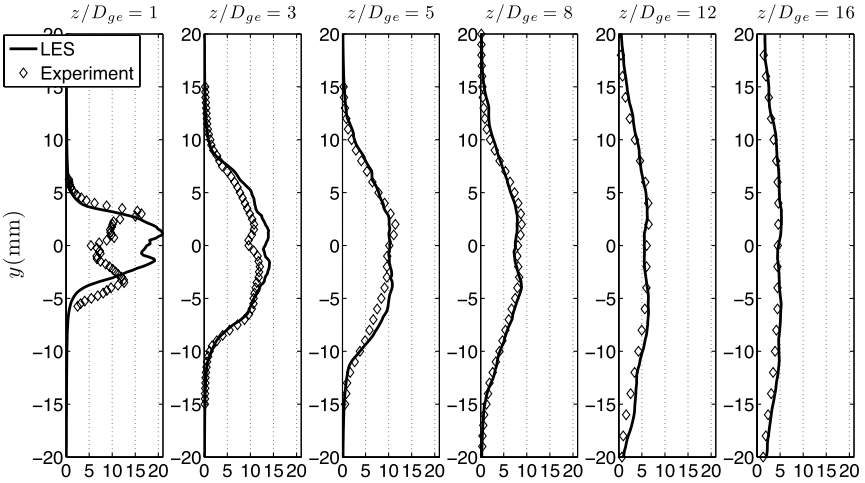

b) U_{hw}^{RMS}

Fig. 10 Profiles of mean velocity (top) and rms velocity (bottom) at $x = 0$ for (SW2). Comparison between LES and experiment.

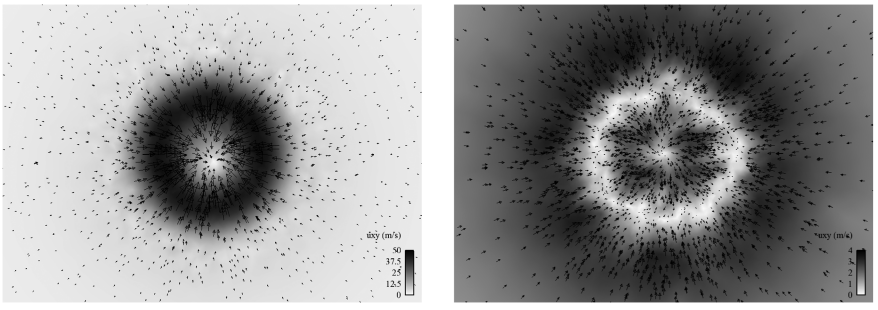

a) z/D_{ge} **= 0.75** **b)** z/D_{ge} **= 4**

Fig. 11 LES of (Coax). Intensity and vector field of U_{xy}, the mean velocity projected on the plane.

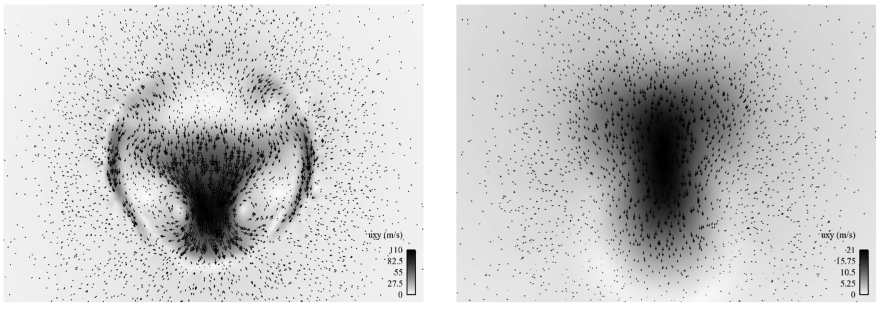

a) z/D_{ge} **= 0.75** **b)** z/D_{ge} **= 4**

Fig. 12 LES of (Dev). Intensity and vector field of the mean velocity projected on the plane U_{xy}.

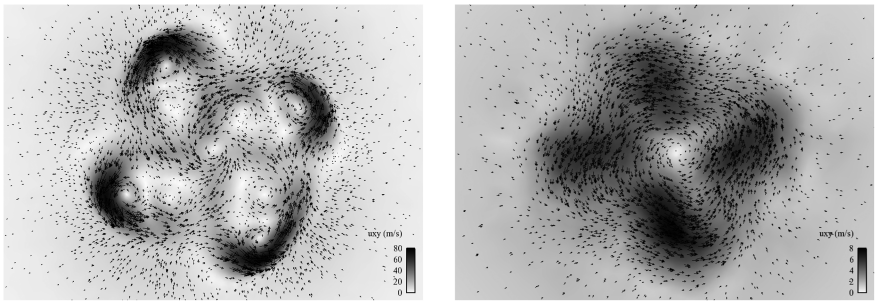

a) z/D_{ge} = 0.75 b) z/D_{ge} = 4

Fig. 13 LES of (Sw). Intensity and vector field of the mean velocity projected on the plane U_{xy}.

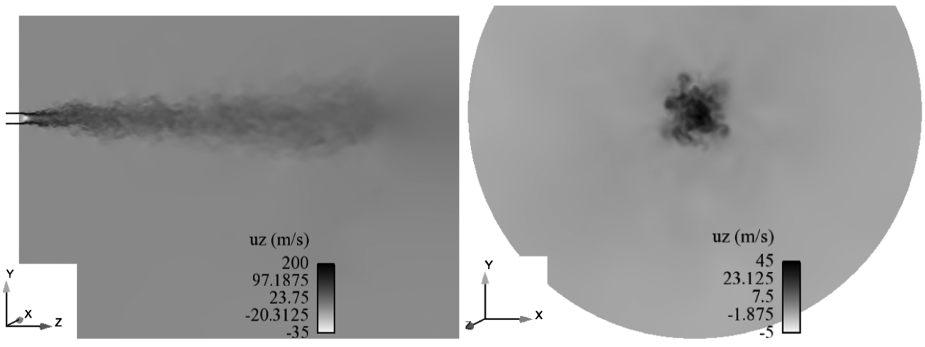

a) u_z: planes x = 0 (left) and z/D_{ge} = 16 (right)

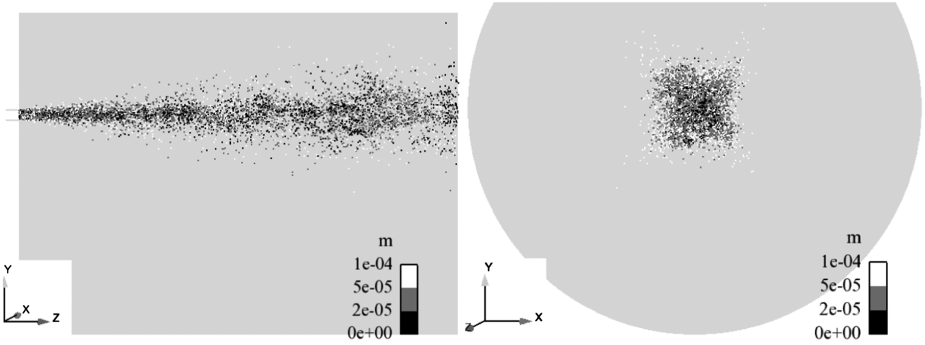

b) Droplets distribution: planes x = 0 (left) and z/D_{ge} = 16 (right)

Fig. 14 LES instantaneous snapshots of axial gas velocity fields u_z and spray droplets for the configuration (Coax): a) axial gas velocity in $x = 0$ (left) and $z/D_{ge} = 16$ (right), b) spray droplets in $x = 0$ (left) and $z/D_{ge} = 16$ (right): the color scale corresponds to the diameter classes : 1) $d_p < 20$ μm (black), 2) 20 μm $\leq d_p <$ 50 μm (gray), and 3) 50 μm $\leq d_p <$ 100 μm (white).

where D_{10}^i and W_p^i are, respectively, the mean diameter and the mean axial velocity of the size class $i = 1), 2), 3)$ and $\sigma = 7.3 \cdot 10^{-2}$ N/m is the surface tension between water and air. Figure 15 shows the evolution of the maximal Weber number $We_{\max}(z)$ obtained from LES in each transverse section of the jet for the three size classes. The Weber number decreases rapidly with downstream distance and never exceeds the critical value of secondary breakup ($We_c = 12$) for droplets with a diameter $d_p < 50$ μm. If $d_p \geq 50$ μm, We can become greater than 12 for $z/D_{ge} \leq 1$ and secondary breakup may occur, especially in the gas shear layer surrounding the droplet injection volume. However, the zone where $We > 12$ is small and it is not clear that large droplets will have the time to break up in this region. In most of the flow, $We \ll 12$ and the assumption of negligible secondary atomization is satisfied.

The effects of control can then be studied by comparing configuration (Coax), (Dev), and (Sw). Figures 16 and 17 display LES instantaneous snapshots in the planes $x = 0$ (left) and $z/D_{ge} = 16$ (right) for the controlled configurations (Dev) and (Sw). Figures 16a and 17a show the axial gas velocity contours. Figures 16b and 17b present the corresponding snapshots for spray droplets. The colors of the size classes are the same as Fig. 14b. Without control (Coax)

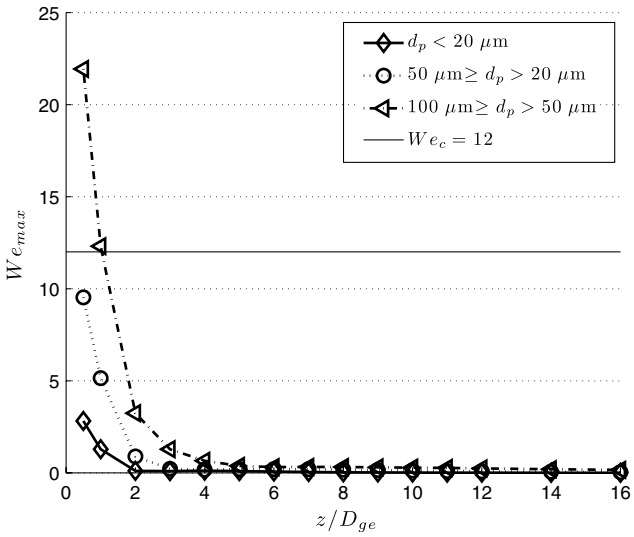

Fig. 15 Maximal local Weber number $We_{\max}$ computed with LES for the three droplet size classes (Coax).

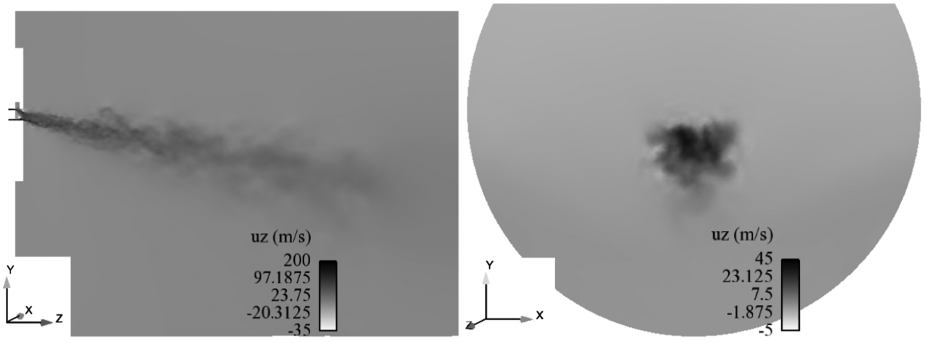

a) u_z: planes $x = 0$ (left) and $z/D_{ge} = 16$ (right)

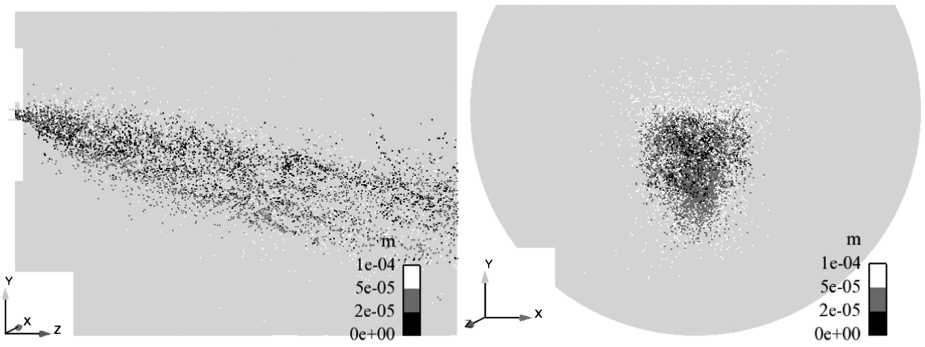

b) Droplets distribution: planes $x = 0$ (left) and $z/D_{ge} = 16$ (right)

Fig. 16 LES instantaneous snapshots of axial gas velocity fields u_z and spray droplets for the configuration (Dev): a) axial gas velocity in $x = 0$ (left) and $z/D_{ge} = 16$ (right), b) spray droplets in $x = 0$ (left) and $z/D_{ge} = 16$ (right): the color scale corresponds to the diameter classes: 1) $d_p < 20$ μm (black), 2) 20 μm $\leq d_p < 50$ μm (gray), and 3) 50 μm $\leq d_p < 100$ μm (white).

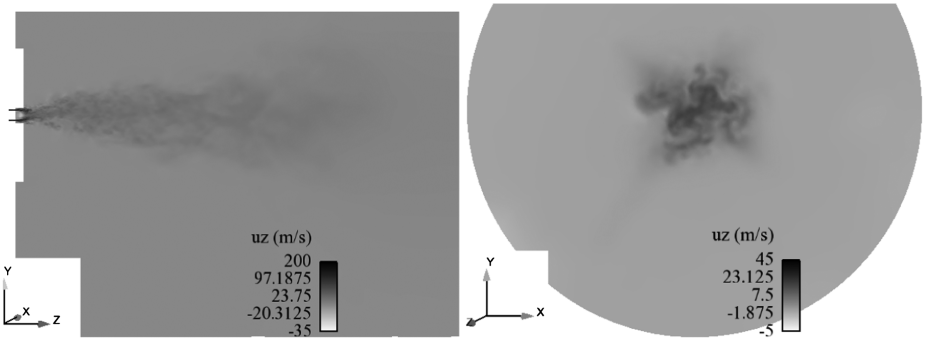

a) u_z: planes $x = 0$ (left) and $z/D_{ge} = 16$ (right)

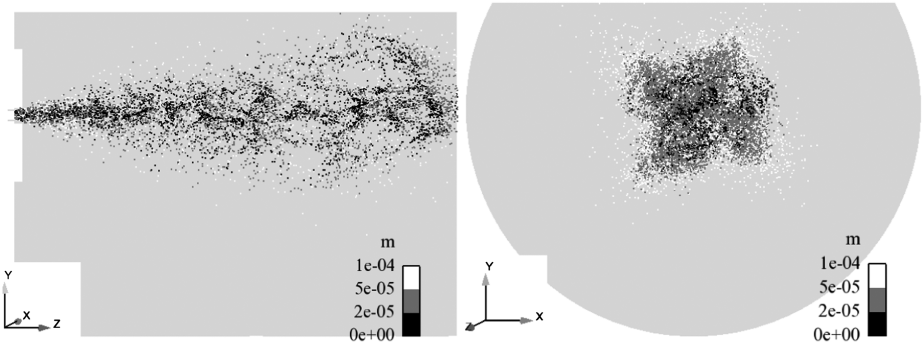

b) Droplets distribution: planes $x = 0$ (left) and $z/D_{ge} = 16$ (right)

Fig. 17 LES instantaneous snapshots of axial gas velocity fields u_z and spray droplets for the configuration (Sw): a) axial gas velocity in $x = 0$ (left) and $z/D_{ge} = 16$ (right), b) spray droplets in $x = 0$ (left) and $z/D_{ge} = 16$ (right): the color scale corresponds to the diameter classes: 1) $d_p < 20$ μm (black), 2) 20 μm $\leq d_p < 50$ μm (gray), and 3) 50 μm $\leq d_p < 100$ μm (white).

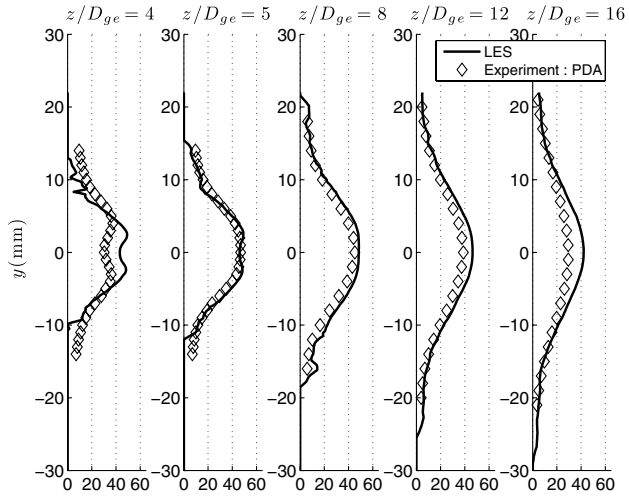

a) W_p **(m/s)**

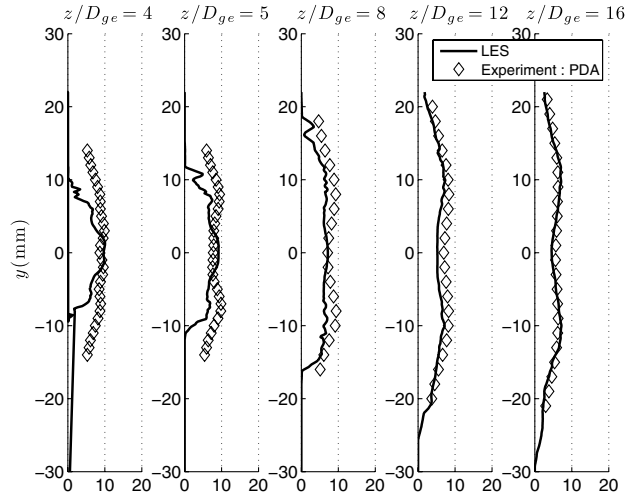

b) W_p^{RMS} **(m/s)**

Fig. 18 (Coax) 20 μ**m** $< d_p <$ **50** μ**m: Radial profiles of mean (top) and rms (bottom) axial particle velocity at** $x = 0$**. Comparison between LES and experiment.**

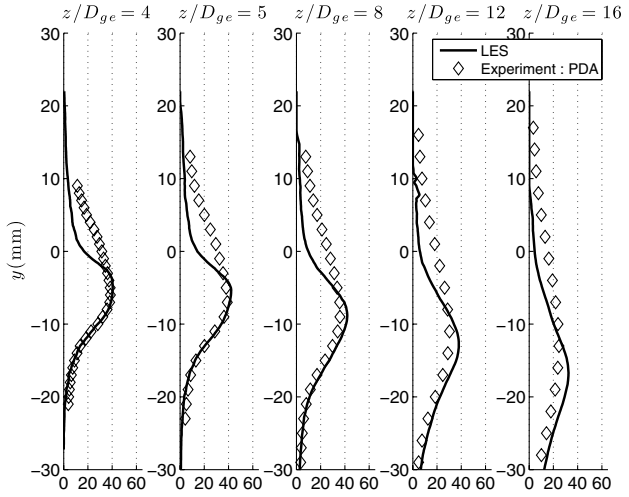

a) W_p **(m/s)**

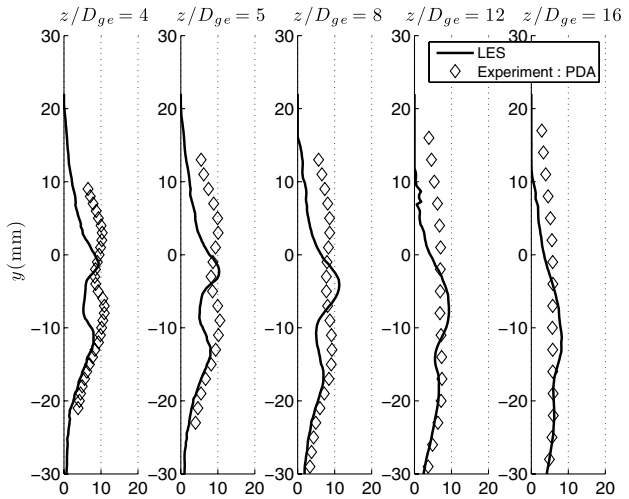

b) W_p^{RMS} **(m/s)**

Fig. 19 (Dev) 20 μ**m** $< d_p <$ **50** μ**m: Radial profiles of mean (top) and rms (bottom) axial particle velocity at** $x = 0$**. Comparison between LES and experiment.**

[Fig. 14], the spray has a low spreading angle without peculiar structures suggesting a limited interaction between the gas turbulence and the dispersed phase: droplets remain inertial in most of the flow. The impacting jet actuator in the configuration (Dev) shifts both gas and droplets (Fig. 16). Control also increases the spray expansion for this configuration. Finally in case (Sw), clusters of droplets are visible showing that interaction between droplets and turbulence is increased by swirl. The spreading angle of the spray also increases significantly compared with the configuration (Coax).

B. Effect of Control on Droplet Velocities

Figures 18–20 compare LES predictions to experimental data for transverse profiles of mean and rms droplets velocity W_p and W_p^{RMS} for the size class 2) and each configuration (Coax), (Dev), and (Sw). The overall agreement is good[‡]. Concerning the (Coax) configuration (Fig. 18), the shapes and expansion of the radial profiles of mean velocity are well reproduced. For example, experimental profiles for $z/D_{ge} < 5$ present a local minimum for W_p: close to the injector, droplets entrained by the high-velocity gas layer surrounding the liquid core are more accelerated than in the center of the spray. LES captures this phenomenon correctly. Root mean square levels are also well reproduced. Differences appear around the spray where W_p^{RMS} obtained with LES falls to zero too fast for $z/D_{ge} \leq 5$. This difference vanishes in the far field.

Concerning the impacting configuration (Dev) [Fig. 19], the levels and positions of the maximum mean velocity are well predicted by LES. But on the actuation side, the mean velocity falls too fast to zero. Conclusions are similar for the rms velocity (Fig. 19b): maxima are well predicted by LES but the position of the maximum on the actuation side is not well obtained. This discrepancy can be explained by the injection model for the dispersed phase (Sec. II.C.4): all LES use the same geometry and the same boundary conditions for droplet injection. However, the actuator may modify both the liquid core shape and the velocity of the injected droplets, a mechanism which is very difficult to characterize experimentally and was simply neglected here.

Like for the gas, the spray vectoring can be evaluated from the position of the maximal droplet velocity. Table 6 presents the shift angle α_p^{Dev} for the three size classes: both LES and experiment show that the velocity fields of all droplets classes are shifted by the same amount when control (Dev) is on. The value of α_p^{Dev} is around 12°, which is a little smaller than the vectoring angle of the single-phase coaxial jet α_g^{Dev} for the same control parameter $R_{\mathrm{ac}} = 0.2$ (Sec. III.A).

Concerning the configuration (Sw) [Fig. 20], swirl effects are well described by LES in terms of shapes and expansion of the mean and

[‡]The comparisons between LES and experiment for the size classes 1 and 3 are not discussed in this paper but are available in the Ph.D. Dissertation of N. Guézennec [47]. They lead to similar conclusions as class 2.

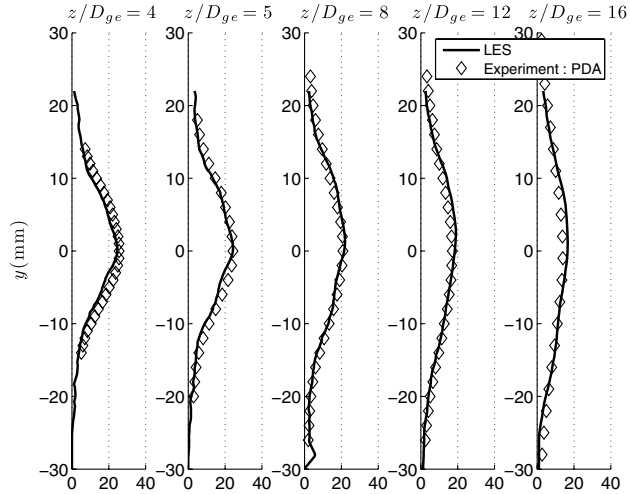

a) W_p **(m/s)**

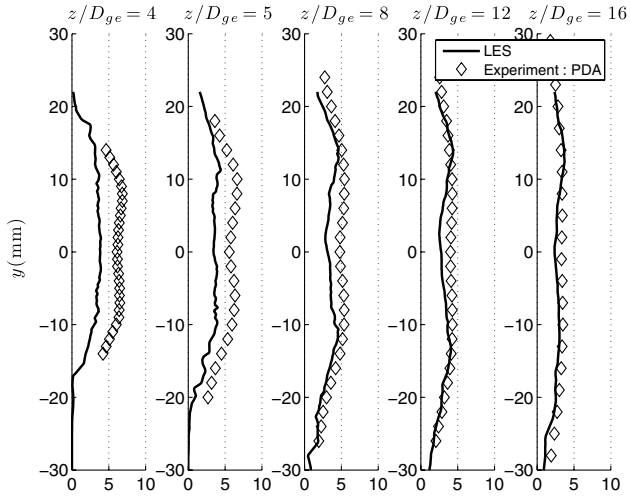

b) W_p^{RMS} **(m/s)**

Fig. 20 (Sw) 20 μm $< d_p <$ 50 μm: Radial profiles of mean (top) and rms (bottom) axial particle velocity at $x = 0$. Comparison between LES and experiment.

rms velocity profiles. Table 6 presents the overexpansion ratio λ_p^{Sw} [Eq. (11)] for the three classes at $z/D_{ge} = 12$. All droplets are more dispersed by the introduction of swirl but not by the same amount: λ_p^{Sw} decreases from 0.5 to 0.3 when droplet sizes increase. The time scale for the swirling motion of the gas can be evaluated by

$$\tau_g^{\mathrm{Sw}} = \frac{R^{\max}}{U_\theta^{\max}} \tag{13}$$

Table 6 Effect of control on the spray: vectoring angle α_p^{Dev} for the (Dev) case and overexpansion ratio λ_p^{Sw} [Eq. (11)] for the (Sw) case

(Dev)	α_p^{Dev}(°)	
Size class	Experiment	LES
0–20 μm	11	13
20–50 μm	11	12
50–100 μm	11	12
(Sw)	λ_p^{Sw}	
Size class	Experiment	LES
0–20 μm	0.50	0.54
20–50 μm	0.4	0.33
50–100 μm	0.32	0.3

where $U_\theta^{\max}$ and $R^{\max}$ are, respectively, the maximal mean tangential gas velocity and the radial position of this maximum. For $z/D_{ge} = 4$, the LES gives $\tau_g^{\mathrm{Sw}} = 0.8$ ms, which is greater than the turbulent time scale τ_g [Eq. (9)]. For particles with diameters $d_p = 10$ and 20 μm, the values of the Stokes number based on this time scale St^{Sw} are, respectively, 0.38 and 1.6. This explains why small droplets in class 1 follow the swirling motion and are more dispersed than the bigger size classes.

C. Effect of Control on the Diameter Distribution

To understand the effect of control on the granulometry in the spray, a joint postprocessing of experimental instantaneous PDA measurements and LES instantaneous droplet realizations was used to evaluate the number-based size distribution function $f_n(d_p)$ along the jet axis. In the LES, droplets were sampled in cylindrical boxes whose positions are shown on Fig. 21. For (Coax) and (Sw), the jet axis is **z**. For (Dev), the jet axis corresponds to the position of the maxima of the axial droplet mean velocity. The length and the radius of each box are respectively $\Delta z = 4$ mm and $\Delta r = 2$ mm. These dimensions enable to sample between 1000 and 3000 droplets per box. To improve convergence, the operation is repeated on 12 droplet instantaneous realizations separated with a time delay $\Delta t = 2.5$ ms. For a droplet with a velocity equal to 10 m/s, this duration corresponds to a displacement of 25 mm , which ensures the independence of the samples in a given box. Concerning experiment, all PDA measurements of the instantaneous droplet diameter d_p included in a box were gathered to account for the local variation in this box.

Figure 22 presents the evolution of f_n along the jet axis for (Coax). LES and experiment are compared with the log-normal distribution f_n^{inj} used in the injection volume (Sec. II.C.4). Agreement between LES and experiment is good: the reduction of proportion of large droplets ($d_p > 40$ μm) when z increases, is captured by LES. This phenomenon could be analyzed as a secondary breakup effect. However, LES does not include any secondary atomization model so that this phenomenon is certainly due to the difference of response of droplets to the carrier gas flow: large droplets with high Stokes numbers are ejected more rapidly than small droplets towards the surrounding air [48]. Figures 23 and 24 present the evolution of f_n for (Dev) and (Sw). Conclusions are similar for big droplets. Their proportion decreases when z increases for the two configurations. But an overestimation of the smallest droplets must also be noticed for LES. This discrepancy may be explained by the lack of collision and coalescence model in the LES. This problem does not occur in the simulations of (Coax) [Fig. 22]. This may suggest that actuators increase coalescence in the spray.

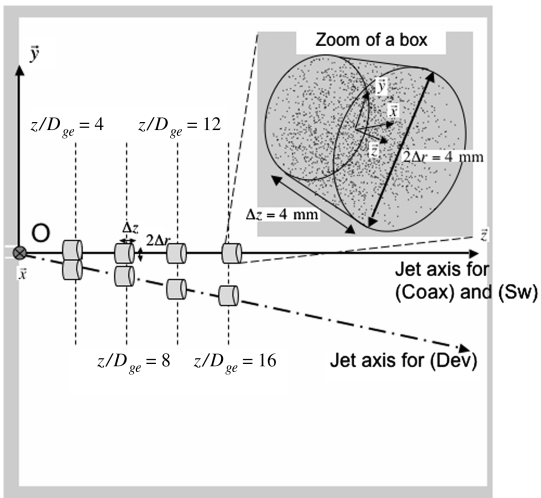

Fig. 21 Methodology to compute the number-based size distribution function for the droplet diameters $f_n(d_p)$: view of computation domain with the positions and the dimensions of the sampling boxes.

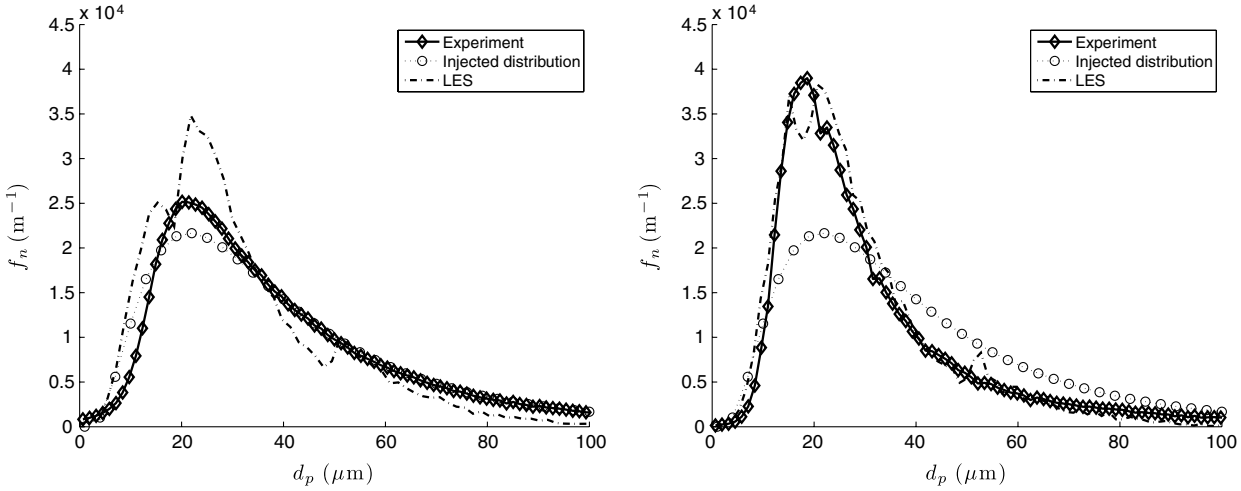

a) $z/D_{ge} = 4$ **b)** $z/D_{ge} = 16$

Fig. 22 Evolution of $f_n(d_p)$ along the jet axis for (Coax).

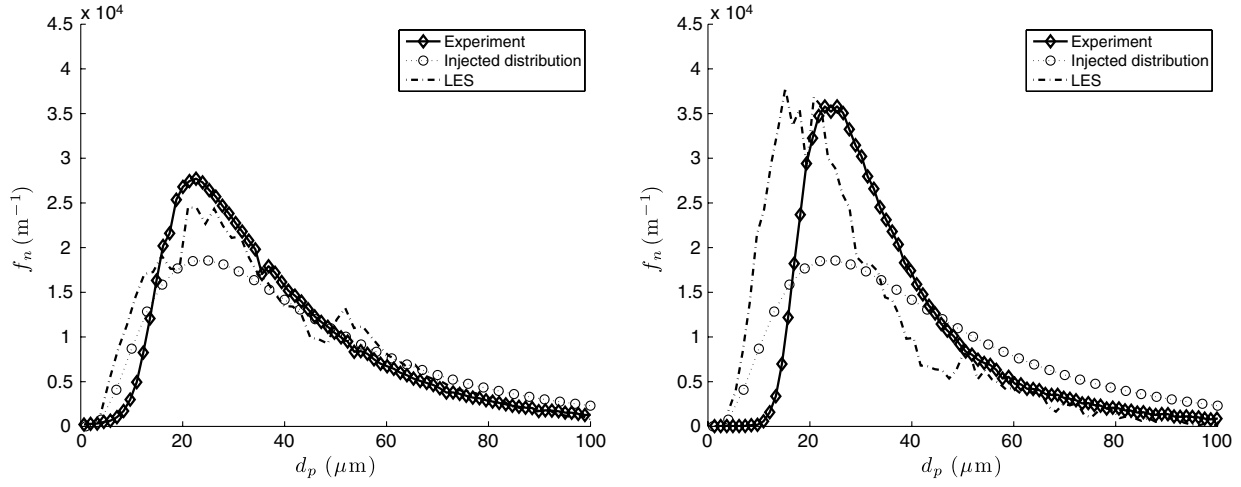

a) $z/D_{ge} = 4$, y = -5*mm* **b)** $z/D_{ge} = 16$, y = -18*mm*

Fig. 23 Evolution of $f_n(d_p)$ along the jet axis for (Dev).

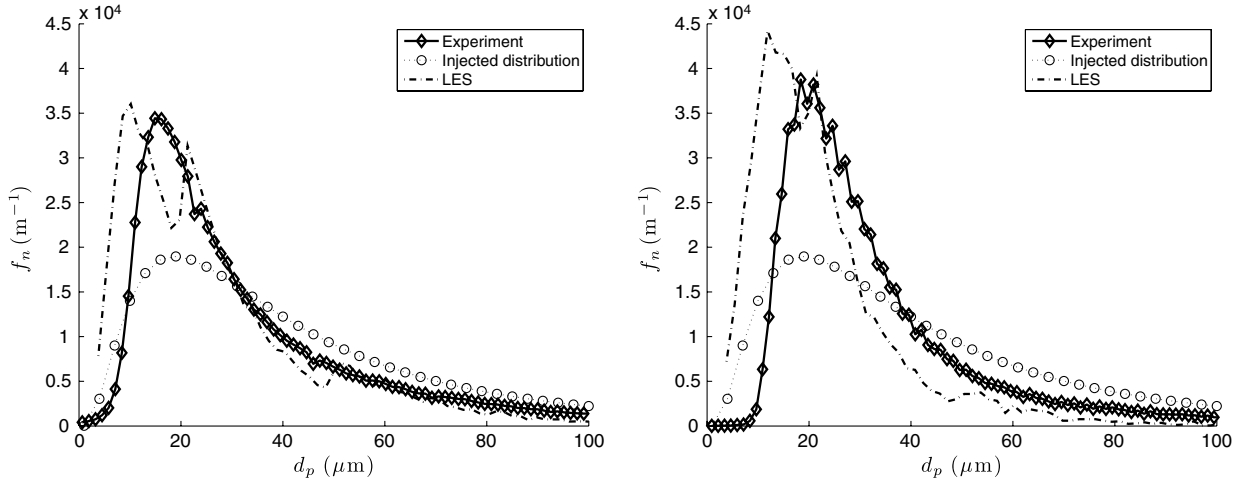

a) $z/D_{ge} = 4$ **b)** $z/D_{ge} = 16$

Fig. 24 Evolution of $f_n(d_p)$ along the jet axis for (Sw).

V. Conclusions

Active control of an air-assisted coaxial spray was studied using LES and experimental methods for two types of actuators: the first one is used to vector the spray while the second one introduces swirl into the spray jet to increase its spreading rate. Both actuators use small rectangular jets placed in the outlet plane of the spray coaxial injector. Results show that LES is able to predict the flow field for the gas and the droplets with and without control. LES also helps to understand the mechanisms affecting the controlled spray: coherent structures are induced by the actuation jets and modify the gaseous flow, generating droplet movements and segregation which depend on the droplet size. For the actuator changing the spray direction (Dev), at a control parameter (actuation flow rate divided by total air flow rate) of 20%, the gas flow can be shifted by 15 deg and droplets by 12 deg. For the swirling actuator (Sw), at a control parameter of 40%, the spreading rate of the gaseous jet increases by 40% and the spray by 30–50% compared with the uncontrolled case while the droplets cloud diameter increases by only 16%. This suggests that these actuation devices can be effective control devices in real combustors. The comparison of size distributions obtained with LES and experiment also suggest that the controlled flows are submitted to more collisions and coalescence mechanisms.

Acknowledgments

This work was supported by Centre de Recherche Claude-Delorme of Air Liquide, Jouy en Josas, France. The authors thank the Centre Européen de Recherche et de Formation Avancée en Calcul Scientifique computational fluid dynamics team staff for their scientific and technical support about the computational fluid dynamics code AVBP. The authors would also like to acknowledge the help of M. Garcia and G. Staffelbach from CERFACS for multiple discussions on large eddy simulation. This work was granted access to the High-Performance Computing resources of Centre de Calcul Recherche et Technologie/Centre Informatique National de l'Enseignement Supérieur/Institut du Développement et des Ressources en Informatique Scientifique under the allocation 2009–x2009025046 made by Grand Equipement National de Calcul Intensif.

References

[1] Candel, S., "Combustion Instabilities Coupled by Pressure Waves and Their Active Control," *24th International Symposium on Combustion*, The Combustion Institute, Pittsburgh, PA, 1992, pp. 1277–1296.

[2] McManus, K., Poinsot, T., and Candel, S., "A Review of Active Control of Combustion Instabilities," *Progress in Energy and Combustion Science*, Vol. 19, 1993, pp. 1–29. doi:10.1016/0360-1285(93)90020-F

[3] Viets, H., "Flip-Flop Jet Nozzle," *AIAA Journal*, Vol. 13, No. 10, 1975, pp. 1375–1379. doi:10.2514/3.60550

[4] Yu, K., Wilson, K. J., Parr, T. P., and Shadow, K. C., "Active Combustion Control in Liquid-Fueled Model Ramjet," *JANNAF 33rd Combustion Subcommittee Meeting*, JANNAF, Monterey, CA, 1996.

[5] Shavit, U., and Chigier, N., "Development and Evaluation of a New Turbulence Generator for Atomization Research," *Experiments in Fluids*, Vol. 20, 1996, pp. 291–301. doi:10.1007/BF00192674

[6] Smith, B., and Glezer, A., "Jet Vectoring Using Synthetic Jets," *Journal of Fluid Mechanics*, Vol. 458, 2002, pp. 1–34. doi:10.1017/S0022112001007406

[7] Dandois, J., "Contrôle des Décollements par Jet Synthétique," Ph.D. Thesis, Université Pierre et Marie Curie, Paris, 2007.

[8] Luo, Z.-b., Xia, Z.-x., and Liu, B., "New Generation of Synthetic Jet Actuators," *AIAA Journal*, Vol. 44, No. 10, 2006, pp. 2418–2420. doi:10.2514/1.20747

[9] Karnawat, J., and Kushari, A., "Controlled Atomization Using a Twin Fluid Atomizer," *Experiments in Fluids*, Vol. 41, No. 4, 2006, pp. 649–663. doi:10.1007/s00348-006-0191-0

[10] Pitsch, H., "Large Eddy Simulation of Turbulent Combustion," *Annual Review of Fluid Mechanics*, Vol. 38, No. 1, 2006, pp. 453–482. doi:10.1146/annurev.fluid.38.050304.092133

[11] Poinsot, T., and Veynante, D., *Theoretical and Numerical Combustion*, 2nd ed., R. T. Edwards, Philadelphia, PA, 2005.

[12] Mare, F. D., Jones, W. P., and Menzies, K., "Large Eddy Simulation of a Model Gas Turbine Combustor," *Combustion and Flame*, Vol. 137, No. 3, 2004, pp. 278–295. doi:10.1016/j.combustflame.2004.01.008

[13] Staelbach, G., Gicquel, L., Boudier, G., and Poinsot, T., "Large Eddy Simulation of Self-Excited Azimuthal Modes in Annular Combustors," *Proceedings of the Combustion Institute*, Vol. 32, No. 2, 2009, pp. 2909–2916. doi:10.1016/j.proci.2008.05.033

[14] Boileau, M., Pascaud, S., Riber, E., Cuenot, B., Gicquel, L., Poinsot, T., and Cazalens, M., "Investigation of Two-Fluid Methods for Large Eddy Simulation of Spray Combustion in Gas Turbines," *Flow, Turbulence and Combustion*, Vol. 80, No. 3, 2008, pp. 291–321.

[15] Moin, P., and Apte, S. V., "Large-Eddy Simulation of Realistic Gas Turbine Combustors," *AIAA Journal*, Vol. 44, No. 4, 2006, pp. 698–708. doi:10.2514/1.14606

[16] Patel, N., and Menon, S., "Simulation of Spray-Turbulence-Flame Interactions in a Lean Direct Injection Combustor," *Combustion and Flame*, Vol. 153, Nos. 1–2, 2008, pp. 228–257. doi:10.1016/j.combustflame.2007.09.011

[17] Farago, Z., and Chigier, N., "Morphological Classification of Disintegration of Round Liquid Jets in a Coaxial Air Stream," *Atomization and Sprays*, Vol. 2, 1992, pp. 137–153.

[18] Bruun, H. H., *Hot-Wire Anemometry. Principles and Signal Analysis*, Oxford Science Publications, Oxford, England, 1995.

[19] Selle, L., "Simulation aux Grandes échelles des Interactions Flamme-Acoustique Dans un écoulement Vrillé," Ph.D. Thesis, INP Toulouse, 2004.

[20] Schmitt, P., Poinsot, T., Schuermans, B., and Geigle, K. P., "Large-Eddy Simulation and Experimental Study of Heat Transfer, Nitric Oxide Emissions and Combustion Instability in a Swirled Turbulent High-Pressure Burner," *Journal of Fluid Mechanics*, Vol. 570, 2007, pp. 17–46. doi:10.1017/S0022112006003156

[21] Smagorinsky, J., "General Circulation Experiments with the Primitive Equations: 1. The Basic Experiment," *Monthly Weather Review*, Vol. 91, No. 3, 1963, pp. 99–164. doi:10.1175/1520-0493(1963)091<0099:GCEWTP>2.3.CO;2

[22] Poinsot, T., and Lele, S., "Boundary Conditions for Direct Simulations of Compressible Viscous Flows," *Journal of Computational Physics*, Vol. 101, No. 1, 1992, pp. 104–129. doi:10.1016/0021-9991(92)90046-2

[23] Maxey, M. R., "The Gravitational Settling of Aerosol Particles in Homogeneous Turbulence and Random Flow Fields," *Journal of Fluid Mechanics*, Vol. 174, No. -1, 1987, pp. 441–465. doi:10.1017/S0022112087000193

[24] Gatignol, R., "The Faxén Formulae for a Rigid Particle in an Unsteady Non-Uniform Stokes Flow," *Journal of Theoretical and Applied Mathematics*, Vol. 1, No. 2, 1983, pp. 143–160.

[25] Sundaram, S., and Collins, L. R., "Numerical Considerations in Simulating a Turbulent Suspension of Finite-Volume Particles," *Journal of Computational Physics*, Vol. 124, No. 2, 1996, pp. 337–350. doi:10.1006/jcph.1996.0064

[26] Hopkins, M., and Louge, M., "Inelastic Microstructure in Rapid Granular Flows of Smooth Disks," *Physics of Fluids*, Vol. 3, 1991, pp. 47–57. doi:10.1063/1.857863

[27] Fede, P., and Simonin, O., "Numerical Study of the Subgrid Fluid Turbulence Effects on the Statistics of Heavy Colliding Particles," *Physics of Fluids*, Vol. 18, No. 4, 2006, pp. 045103–045117.

[28] Wunsch, D., Fede, P., and Simonin, O., "Development and Validation of a Binary Collision Detection Algorithm for Polydispersed Particle Mixture," *2008 ASME Fluids Engineering Conference*, American Society of Mechanical Engineers, Fairfield, NJ, 2008.

[29] Boivin, M., Simonin, O., and Squires, K. D., "Direct Numerical Simulation of Turbulence Modulation by Particles in Isotropic Turbulence," *Journal of Fluid Mechanics*, Vol. 375, 1998, pp. 235–263. doi:10.1017/S0022112098002821

[30] Vermorel, O., "Étude Numérique et Modélisation de la Turbulence dans un écoulement de Nappe Chargée en Particules," Ph.D. Thesis, INP Toulouse, 2003.

[31] Elghobashi, S., and Truesdell, G., "On the Two-Way Interaction Between Homogeneous Turbulence and Dispersed Solid Particles," *Physics of Fluids*, Vol. 5, No. 7, 1993, pp. 1790–1801.

[32] Squires, K. D., and Eaton, J. K., "Particle Response and Turbulence Modification in Isotropic Turbulence," *Physics of Fluids*, Vol. 2, No. 7,

1990, pp. 1191–1203.
[33] Miller, R., and Bellan, J., "Direct Numerical Simulation and Subgrid Analysis of a Transitional Droplet Laden Mixing Layer," *Physics of Fluids*, Vol. 12, No. 3, 1999, pp. 650–671.
[34] Schiller, L., and Nauman, A., "A Drag Coefficient Correlation," *VDI Zeitung*, Vol. 77, 1935, pp. 318–320.
[35] Maxey, M., and Riley, J., "Equation of Motion for a Small Rigid Sphere in a Nonuniform Flow," *Physics of Fluids*, Vol. 26, No. 4, 1983, pp. 883–889.
[36] Wang, Q., and Squires, K. D., "Large Eddy Simulation of Particle-Laden Turbulent Channel Flow," *Physics of Fluids*, Vol. 8, No. 5, 1996, pp. 1207–1223.
[37] Yamamoto, Y., Pottho, M., Tanaka, T., Kajishima, T., and Tsuji, Y., "Large-Eddy Simulation of Turbulent Gas-Particle Flow in a Vertical Channel: Effect of Considering Inter-Particle Collisions," *Journal of Fluid Mechanics*, Vol. 442, 2001, pp. 303–334. doi:10.1017/S0022112001005092
[38] Apte, S., Mahesh, K., Moin, P., and Oefelein, J., "Large-Eddy Simulation of Swirling Particle-Laden Flows in a Coaxial-Jet Combustor," *International Journal of Multiphase Flow*, Vol. 29, No. 8, 2003, pp. 1311–1331. doi:10.1016/S0301-9322(03)00104-6
[39] Smirnov, A., Shi, S., and Celik, I., "Random Flow Generation Technique for Large Eddy Simulations and Particle-Dynamics Modeling," *Journal of Fluids Engineering*, Vol. 123, No. 2, 2001, pp. 359–371. doi:10.1115/1.1369598
[40] Kraichnan, R., "Diffusion by a Random Velocity Field," *Physics of Fluids*, Vol. 13, 1970, pp. 22–31.
[41] Guézennec, N., and Poinsot, T., "Acoustically Non-Reflecting and Reflecting Boundary Conditions for Injection of Vorticity in Compressible Solvers," *AIAA Journal*, Vol. 47, No. 7, 2009, pp. 1709–1722. doi:10.2514/1.41749
[42] Eroglu, H., Chigier, N., and Farago, Z., "Coaxial Atomizer Liquid Intact Length," *Physics of Fluids*, Vol. 3, No. 2, Feb. 1991, pp. 303–308.
[43] Engelbert, C., Hardalupas, Y., and Whitelaw, J., "Breakup Phenomena in Coaxial Airblast Atomizers," *Proceedings: Mathematical and Physical Sciences*, No. 1941, 1995, pp. 189–229.
[44] Porcheron, E., Carreau, J.-L., Le Visage, D., and Roger, F., "Effect of Injection Gas Density on Coaxial Liquid Atomization," *Atomization and Sprays*, Vol. 12, Nos. 1–3, 2002, p. 20.
[45] Gorokhovski, M., and Herrmann, M., "Modeling Primary Atomisation," *Annual Review of Fluid Mechanics*, Vol. 40, No. 1, 2008, pp. 343–366. doi:10.1146/annurev.fluid.40.111406.102200
[46] Celik, I. B., Cehreli, Z. N., and Yavuz, I., "Index of Resolution Quality for Large Eddy Simulations," *Journal of Fluids Engineering*, Vol. 127, Nos. 949–958, 2005.
[47] Guézennec, N., "Contrôle Actif de la Combustion Diphasique," Ph.D. Thesis, Université de Toulouse, 2010.
[48] Fede, P., Février, P., and Simonin, O., "Numerical Study of the Effect of the Fluid Turbulence Microscales on Particle Segregation and Collision in Gas-Solid Turbulent Flows," *5th International Conference on Multiphase Flow*, ICMF, Yokohama, Japan, 2004.

F. Ladeinde
Associate Editor